

Octahedral Coordinated Trivalent Cobalt Enriched Multimetal Oxygen-Evolution Catalysts

Junsheng Chen, Hao Li, Zixun Yu, Chang Liu, Ziwen Yuan, Chaojun Wang, Shenlong Zhao, Graeme Henkelman, Shuzhou Li, Li Wei,* and Yuan Chen*

Octahedral coordinated trivalent cobalt cations ($\text{Co}_{\text{Oh}}^{3+}$) in metal oxyhydroxides are highly active catalytic sites for the oxygen evolution reaction (OER), a critical bottleneck for efficient water splitting; however, previous synthetic methods have limited control over these sites. Herein, a scalable electrodeposition method coupled with in situ oxidation to produce amorphous Co–Fe–W trimetallic oxyhydroxides enriched with $\text{Co}_{\text{Oh}}^{3+}$ is developed. X-ray absorption, in operando spectroscopic analysis, and computational studies reveal that 72% of the Co atoms are present in $\text{Co}_{\text{Oh}}^{3+}$ sites. Fe and W synergistically affect the electronic structure of Co and provide a favorable coordination environment. The Co–Fe–W oxyhydroxide exhibits superior OER catalytic performance with an impressive turnover frequency of 1.96 s^{-1} at an overpotential of 300 mV, a low Tafel slope of 32 mV dec^{-1} , and small activation energy of 53 kJ mol^{-1} in alkaline electrolyte. The catalyst directly deposited on Ni foams can serve as a robust OER electrode in two-electrode water electrolyzers; they deliver a current density of 100 mA cm^{-2} at a small overpotential of 234 mV in alkaline electrolyte with excellent durability under 100 mA cm^{-2} over 120 h. These catalysts are excellent for practical water splitting applications.

1. Introduction

Green hydrogen (H_2) can be produced from water electrolysis as a promising clean fuel to enable a more sustainable society.^[1] Anodic oxygen evolution reaction (OER) in water electrolyzers is slow and requires substantial energy inputs.^[2] Catalysts are necessary to deliver a high current density under a low

overpotential (η) to enable efficient water electrolyzers.^[3] Even the most efficient precious-metal-based catalysts require a substantial overpotential. Researchers have explored cobalt oxide (Co_3O_4), hydroxides ($\text{Co}(\text{OH})_2$), and oxyhydroxides (CoOOH) as catalysts for OER.^[4] It has been found that their catalytic performance correlates with the energetics of OER intermediates on active catalytic Co sites.^[5] The catalytic activity of Co catalysts can be significantly improved by alloying with other metals, such as Fe, Ni, and Mn, which optimizes the Co *d*-orbital electronic structure, enabling more efficient adsorption/desorption of OER intermediates.^[4c,d,6] Recently, several high-valence metal cations, including W^{6+} , Mo^{6+} , and V^{5+} , have been identified as OER performance boosters for Co catalysts because their empty *d*-orbitals can efficiently modulate the electronic structure of Co.^[6d,5c,7] In particular, a Co–Fe–W trimetallic metal oxyhydroxide catalyst exhibits one of the lowest overpotential

(η_{10}) of 191 mV (supported on Au plated Ni foams (NiFs) or 223 mV supported on glassy carbon electrodes) at 10 mA cm^{-2} in alkaline electrolyte, demonstrating a very promising OER catalyst.^[5c] In another study, Fe was found to play a critical role in regulating the catalytic activity of Co–Fe–W oxyhydroxides, and the optimized $\text{W}_{0.5}\text{Co}_{0.4}\text{Fe}_{0.1}$ exhibited an overpotential of 310 mV at 100 mA cm^{-2} .^[7b] Furthermore, recent in situ mechanistic studies suggest that Co catalysts would undergo structure transformations during OER to form CoOOH , in which high valence Co ions in the octahedral coordination ($\text{Co}_{\text{Oh}}^{3+}$) serve as active catalytic sites for OER.^[8] However, the abundance of $\text{Co}_{\text{Oh}}^{3+}$ in the previously reported Co–Fe–W oxyhydroxides was not controlled. Thus, we envision that creating Co–Fe–W oxyhydroxides enriched with $\text{Co}_{\text{Oh}}^{3+}$ may deliver a high-performance catalyst for OER.

A key challenge is how to synthesize Co–Fe–W oxyhydroxides with a high abundance of $\text{Co}_{\text{Oh}}^{3+}$, which have homogeneously dispersed metal components without phase segregation so that different metal atoms can actively interact with each other. The previously used sol–gel method by hydrolyzing the mixture of CoCl_2 , FeCl_3 , and WCl_6 , mainly resulted in Co^{2+} species in the resulting Co–Fe–W oxyhydroxides.^[5c] Hydrothermal synthesis involving WCl_6 often leads to the formation of a segregated WO_x phase due to the spontaneous hydrolysis.^[7b] In comparison, electrodeposition is a versatile technique to synthesize


J. Chen, Z. Yu, C. Liu, Z. Yuan, C. Wang, Dr. S. Zhao, Dr. L. Wei, Prof. Y. Chen

School of Chemical and Biomolecular Engineering
The University of Sydney
Darlington, NSW 2006, Australia

E-mail: l.wei@sydney.edu.au; yuan.chen@sydney.edu.au

Dr. H. Li, Prof. G. Henkelman
Department of Chemistry and the Oden Institute for Computational and Engineering Sciences
The University of Texas at Austin
105 E. 24th Street, Stop A5300, Austin, TX 78712, USA

Prof. S. Li
School of Materials Science and Engineering
Nanyang Technological University
50 Nanyang Avenue, Singapore 639798, Singapore

 The ORCID identification number(s) for the author(s) of this article can be found under <https://doi.org/10.1002/aenm.202002593>.

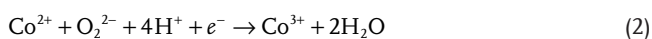
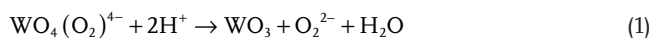
DOI: 10.1002/aenm.202002593

Co catalysts with uniform elemental distribution and tunable structures.^[5a,9] Co catalysts can be deposited on various conductive and mechanically robust porous substrates without polymeric binders. Such porous electrodes can also enable efficient mass transfer for reaction intermediates and generated gases.^[10] Further, an aqueous oxidation method has been used to oxidize Co^{2+} to Co^{3+} through Co Fenton reaction in catalyst synthesis.^[11] Along these lines, we propose that it may be possible to in situ generate Co^{3+} and use it for electrodeposition.

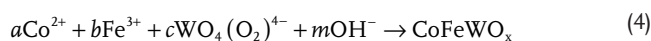
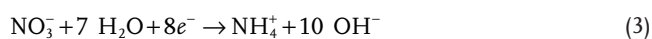
Herein, we demonstrate a fast and scalable electrodeposition method to synthesize amorphous Co–Fe–W oxyhydroxides enriched with $\text{Co}_{\text{OH}}^{3+}$ as a highly efficient OER catalyst. Peroxide ligands released from the $\text{WO}_4(\text{O}_2)^{4-}$ precursor oxidize Co^{2+} to Co^{3+} , which was then electrodeposited together with Fe^{3+} , WO_4^{2-} , and OH^- to form Co–Fe–W oxyhydroxides. Detailed characterization by X-ray absorption spectroscopy (XAS) elucidates local environments and the average valence state of Co atoms in the deposited catalysts. The abundance of Co^{3+} was determined by X-ray photoelectron spectroscopy (XPS), X-ray absorption near edge structure (XANES) analysis, and electron energy loss spectroscopy (EELS). The catalytic performance of synthesized amorphous Co–Fe–W oxyhydroxides was comprehensively examined and compared with several reference catalysts. Further, the in operando electrochemical impedance spectroscopy (EIS), Fourier transformed alternative current voltammetry (FTACV) together with density functional theory (DFT) calculations reveal how Fe and W modulate electronic structures of Co, affording superior OER performance. Finally, using catalysts directly deposited on NiFs as an anode, a two-electrode water electrolyzer demonstrates excellent performance in an alkaline electrolyte and neutral seawater.

2. Results and Discussion

The synthesis of catalysts by the electrodeposition method is illustrated in **Figure 1a**. Experimental details are described in the Experimental Section. Briefly, we prepared an electrodeposition bath by an equimolar mixing of H_2O_2 and Na_2WO_4 to form $\text{WO}_4(\text{O}_2)^{4-}$,^[12] followed by adding $\text{Co}(\text{NO}_3)_2$ and $\text{Fe}(\text{NO}_3)_3$. According to the elemental optimization reported in a previous study,^[7b] the concentration of Co, Fe, and W in the bath solution was set at 20, 5, and 20×10^{-3} M, respectively. The electrodeposition was carried out at -0.2 V versus Ag/AgCl (3 M KCl) for 10 min on cleaned Ni foams (NiFs).^[11] During the electrodeposition, peroxide ligands (O_2^{2-}) released from $\text{WO}_4(\text{O}_2)^{4-}$ oxidize Co^{2+} to Co^{3+} , according to reactions that can be written as:



At the same time, the reduction of NO_3^- ions generates OH^- and leads to the deposition of amorphous tertiary Co–Fe–W oxyhydroxides enriched with Co^{3+} (denoted as CoFeWO_x). The reactions can be expressed as:



We also optimized the electrodeposition time. As shown in **Figure S1a** (Supporting Information), there is a linear relationship between the mass of deposited catalysts on NiFs and the deposition time. Analysis by inductively coupled plasma atomic emission spectroscopy (ICP-AES) shows minor elemental composition changes when the deposition time increases from 2 to 30 min (**Figure S1b**, Supporting Information). OER performance tests (see **Figure S1c,d** and the related discussion in Supporting Information) indicate that 10 min is the optimal deposition time, which was used for the rest of the study.

After electrodeposition, **Figure 1b** shows that pale yellow–green color solids appear on NiFs with a geometric areal mass loading of 0.31 ± 0.06 mg cm^{-2} . Several reference catalysts were also synthesized for comparison. Catalysts with reduced Co^{3+} abundance (denoted as $\text{CoFeWO}_x\text{-R}$) were also synthesized by adding reductive ascorbic acid in the electrodeposition bath (see **Figure S2** and the related discussion in Supporting Information). Ascorbic acid is found to consume peroxide ligands competitively, resulting in a lower Co^{3+} abundance in $\text{CoFeWO}_x\text{-R}$. A crystallized and phase segregated catalyst (denoted as $\text{CoFeWO}_x\text{-A}$) was obtained by thermal annealing CoFeWO_x at 500 °C in Ar for 1 h. Bimetallic (CoFeO_x) and monometallic (CoO_x) were synthesized by electrodeposition under similar experimental conditions (see details in the Experimental Section). Overall, the electrodeposition method is time-efficient. Including the time required to prepare electrodeposition bath electrolytes, it took less than 1 h to complete the whole process. Additionally, this method is scalable for making large electrodes. A large area electrode of 60 cm^2 was fabricated as a demonstration (see the photo in **Figure S3**, Supporting Information).

Various techniques were used to characterize the physicochemical properties of catalysts. Scanning electron microscope (SEM) images shown in **Figure 1c** suggest that CoFeWO_x was deposited uniformly on NiFs. Energy-dispersive X-ray spectroscopy (EDX, **Figure S4**, Supporting Information) analysis indicates a Co: Fe: W atomic ratio of 1.00: 0.95: 1.15, which agrees with results obtained by XPS and ICP-AES (see **Table S1**, Supporting Information). The atomic ratio between Co and Fe in CoFeWO_x is similar to the optimal result reported for Fe–Co based OER electrocatalysts.^[6b] Nitrogen physisorption analysis shows that CoFeWO_x has a Brunauer–Emmett–Teller (BET) surface area of 75.3 m^2 g^{-1} , and the Barrett–Joyner–Halenda (BJH) pore size distribution indicates the existence of mesopores around 5–10 nm (see **Figure S5**, Supporting Information). In conjunction with large macropores in NiFs, the hierarchically porous structure in the $\text{FeCoWO}_x/\text{NiF}$ electrodes is beneficial for OER by providing a large accessible surface area and fast mass transfer for electrolyte ions and gaseous products.^[10,13]

The high-resolution transmission electron microscope (TEM) image in **Figure 1d** shows that CoFeWO_x is composed of thin nanoplates without apparent lattice fringes. The selected area electron diffraction (SAED) analysis in the inset of **Figure 1d** shows no crystalline lattice fringes. X-ray diffraction (XRD) in **Figure S6** (Supporting Information) shows featureless XRD patterns. These results confirm that CoFeWO_x is amorphous. Further, no high-contrast spots were found in the high-angle annular dark-field (HAADF) mode of our scanning

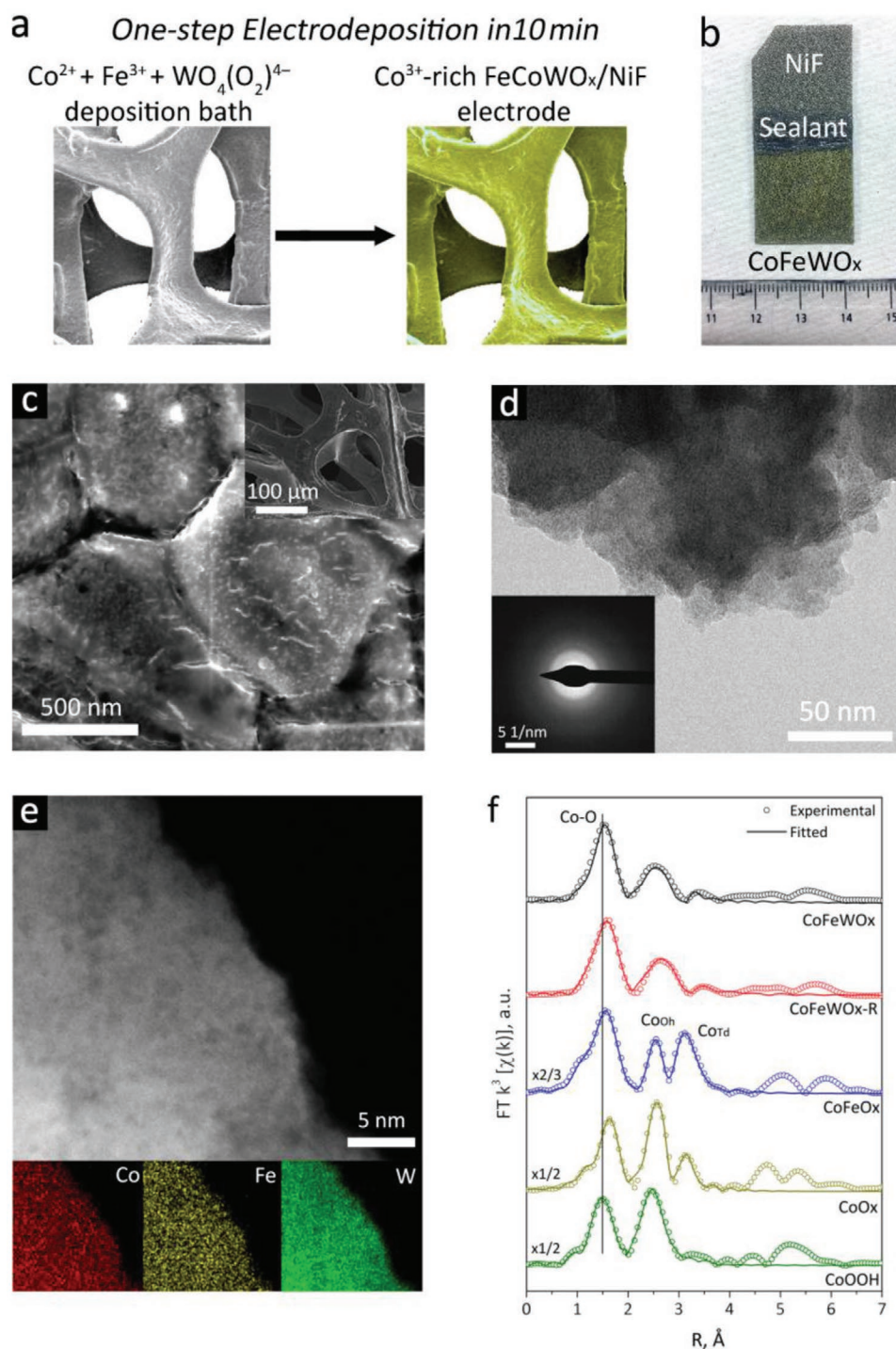


Figure 1. Synthesis and structural characterization of CoFeWO_x . a) A schematic illustration of the electrodeposition of CoFeWO_x on NFs. b) A photo of a NiF electrode with CoFeWO_x deposited on an area of $2 \times 2 \text{ cm}^2$. c) An SEM image of a $\text{CoFeWO}_x/\text{NiF}$ electrode. d) An HRTEM image of CoFeWO_x and its SAED pattern (inset). e) A HAADF-STEM image and the corresponding EDX elemental maps of CoFeWO_x . f) The k^3 -weighted FT-EXAFS spectra of CoFeWO_x and references.

TEM (STEM) analysis, as displayed in Figure 1e. The corresponding EDX maps confirm the uniform elemental distribution in CoFeWO_x . In comparison, XRD and TEM characterization results of $\text{CoFeWO}_x\text{-R}$ (Figure S7, Supporting Information) show structural properties similar to those of CoFeWO_x ,

suggesting that adding ascorbic acid in the electrodeposition bath does not affect the amorphous structure and uniform element distribution in CoFeWO_x . On the contrary, Figure S8 (Supporting Information) shows evident crystal phase segregation in the thermally annealed $\text{CoFeWO}_x\text{-A}$.

XAS was applied to elucidate the coordination environment of Co in CoFeWO_x using extended X-ray absorption fine structure (EXAFS) at the Co K-edge, for comparison with several reference structures. Figure 1f displays the k^3 -weighted Fourier-transformed EXAFS (FT-EXAFS) spectra. The first shell coordination number of Co (CN_{Co}) was obtained by fitting the FT-EXAFS spectra, with results listed in Table S2 (Supporting Information). CoFeWO_x and $\text{CoFeWO}_{x-\text{R}}$ have similar CN_{Co} of 5.8 ± 0.4 and 5.9 ± 0.2 , respectively, indicating that Co atoms mostly occupy octahedral sites (Co_{Oh}).^[5c,8a] In contrast, the EXAFS spectra of CoFeO_x and CoO_x show split peaks at the second Co–Co shell ($R = 2\text{--}3.5 \text{ \AA}$), indicating the co-existence of Co_{Oh} and Co atoms at fourfold tetrahedral sites (Co_{Td}). A linear combination fit reveals that 38 and 74 at% of Co atoms are at Co_{Oh} sites in CoFeO_x and CoO_x , respectively. Additionally, the Co–O bond length of CoFeWO_x at $1.921 \pm 0.012 \text{ \AA}$ is shorter than that of $\text{CoFeWO}_{x-\text{R}}$, CoFeO_x , and CoO_x at 1.977 ± 0.025 , 1.953 ± 0.042 , $2.008 \pm 0.037 \text{ \AA}$, respectively. The contracted Co–O bond length in CoFeWO_x is similar to that of CoOOH at $1.900 \pm 0.011 \text{ \AA}$, suggesting a high average Co valence state in CoFeWO_x .^[5c] XANES and EXAFS of catalysts at the Fe K-edge

were also compared, as displayed in Figure S9 and Table S2 (Supporting Information). Fe atoms situate in the octahedral environment with minimal structural changes between the different catalysts.

Several spectroscopic methods further confirm the formation of abundant Co^{3+} in CoFeWO_x . First, Figure 2a displays the XPS spectra of the catalysts. Their $\text{Co}2p_{3/2}$ peaks can be deconvoluted into contributions from Co^{3+} and Co^{2+} at the binding energy of ≈ 780.2 and 782.2 eV , respectively.^[6c] Due to in situ oxidation by O_2^{2-} , the abundance of Co^{3+} in CoFeWO_x is 72 at%, which is much higher than that in $\text{CoFeWO}_{x-\text{R}}$ (23 at%), CoFeO_x (41 at%), and CoO_x (12 at%). Second, the pre-edge position shift observed in the Co K-edge XANES spectra displayed in Figure S10 (Supporting Information) is consistent with the changing trend of Co^{3+} abundance revealed by XPS. Third, the valence state of Co was quantified by Co L-edge EELS. Figure 2b shows a TEM image of CoFeWO_x with four marked spots at different sample thicknesses. EELS spectra collected at the four spots in Figure 2c show an identical line shape and peak positions for Co L_3 and L_2 edges, suggesting that the valence state of Co is similar at the surface and in the bulk of CoFeWO_x . The L_3

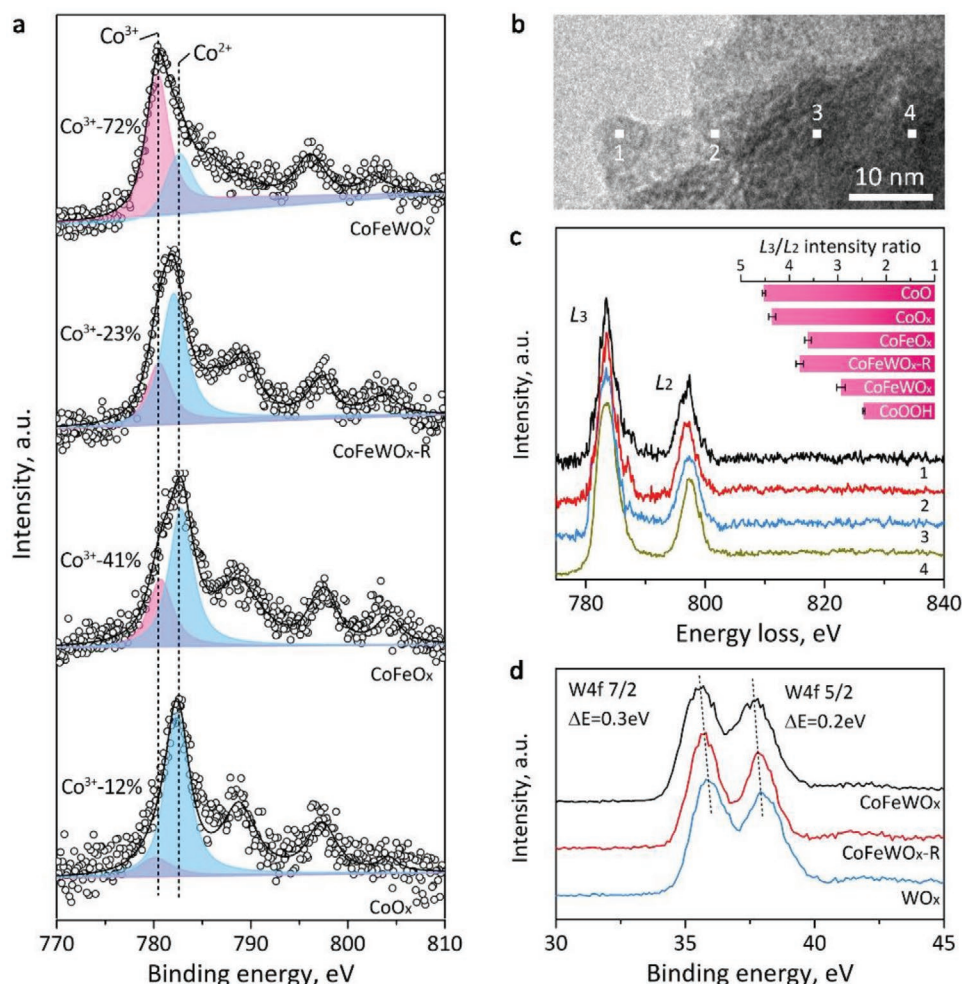


Figure 2. Electronic structures of Co in CoFeWO_x , $\text{CoFeWO}_{x-\text{R}}$, CoFeO_x , and CoO_x catalysts. a) XPS spectra of Co. b) A TEM image of CoFeWO_x with four marked spots at different thicknesses and c) the corresponding Co L-edge EELS spectra collected at the four spots. The inset in (c) shows the calculated Co L_3/L_2 intensity ratios of the catalysts in comparison with CoO and CoOOH references. d) $\text{W}4f$ XPS spectra in CoFeWO_x , $\text{CoFeWO}_{x-\text{R}}$, and WO_x .

and L_2 intensity ratio can be correlated with the valence state of Co.^[14] We calculated the intensity ratio of Co L_3 and L_2 edges for different catalysts and compared them in the inset of Figure 2c. The ratio of CoFeWO_x at 2.93 is higher than 2.46 of CoOOH . A linear interpretation shown in Figure S11 (Supporting Information) indicates that Co in CoFeWO_x has a valence of 2.74, which is similar to the value obtained by the surface sensitive XPS (Figure 2a). In comparison, $\text{CoFeWO}_x\text{-R}$ and CoFeO_x have L_3/L_2 intensity ratios of 3.78 and 3.61 (Figure S11, Supporting Information), corresponding to a Co^{3+} abundance of 30 and 43 at%, respectively. These ratios are close to those determined from the XPS results shown in Figure 2a at 23 and 41 at%. Based on our EXAFS analysis results and spectroscopic valence state assessment of Co, we conclude that all Co^{2+} and Co^{3+} in CoFeWO_x and $\text{CoFeWO}_x\text{-R}$ are at octahedral sites. The Co^{3+} in CoFeO_x (41 at%) would preferentially occupy octahedral sites, agreeing with EXAFS fitting results (38 at%).^[15] Meanwhile, the abundant Co^{2+} in CoO_x (88 at%) would situate at both octahedral and tetrahedral coordination sites.

XPS was also used to examine the electronic structure of W and Fe. Figure 2d shows that $\text{W}4f_{7/2}$ (36.1 eV) and $\text{W}4f_{5/2}$ (38.2 eV) XPS spectra of CoFeWO_x and $\text{CoFeWO}_x\text{-R}$ are about 0.3–0.2 eV lower than that in WO_x . This result is similar to recent reports that W doped in CoOOH resides at lower oxidation states due to substantial structural distortions from Co sites.^[5c,7c] Meanwhile, $\text{Fe}2p$ XPS spectra of CoFeWO_x , $\text{CoFeWO}_x\text{-R}$, and CoFeO_x are comparable with that of Fe_2O_3

(Figure S12, Supporting Information), indicating that Fe^{3+} is the dominate Fe species.^[6b] Further, the deconvolution of O1s XPS spectra confirms the co-existence of M–O and M–OH bonds. Detailed deconvolution analysis further proves that they exhibit a similar level of O vacancies (see Figure S13 and the related discussion in Supporting Information). Thus, we rule out that oxygen vacancy would play a significant role in their observed different OER performance.

The catalytic performance for OER was evaluated by depositing catalysts (removed from NiFs) on rotating disk glassy carbon electrodes (GCEs) with an areal mass loading of 0.2 mg cm^{-2} in a three-electrode configuration in O_2 saturated 1 M KOH electrolytes. Figure 3a displays linear sweep voltammetry (LSV) polarization curves collected under a scan rate of 2 mV s^{-1} . Among the tested catalysts and references, CoFeWO_x exhibits the highest catalytic activity with the lowest overpotential (η_{10}) of 231 mV at 10 mA cm^{-2} , which is lower than that of $\text{CoFeWO}_x\text{-R}$ at 249 mV, CoFeO_x at 303 mV, and commercial RuO_2 at 324 mV (see Table 1). After thermal annealing at 500°C , the phase-segregated $\text{CoFeWO}_x\text{-A}$ shows significantly reduced activity with η_{10} at 332 mV, suggesting that amorphous crystallinity is important for the observed high catalytic activity of CoFeWO_x . We further normalized our measured current densities from the catalysts based upon their electrochemically active surface area (ECSA). The ECSA was determined by measuring the double-layer capacitance (C_{dl}) of the catalysts, as shown in Figure S14 and Table S3 (Supporting Information).

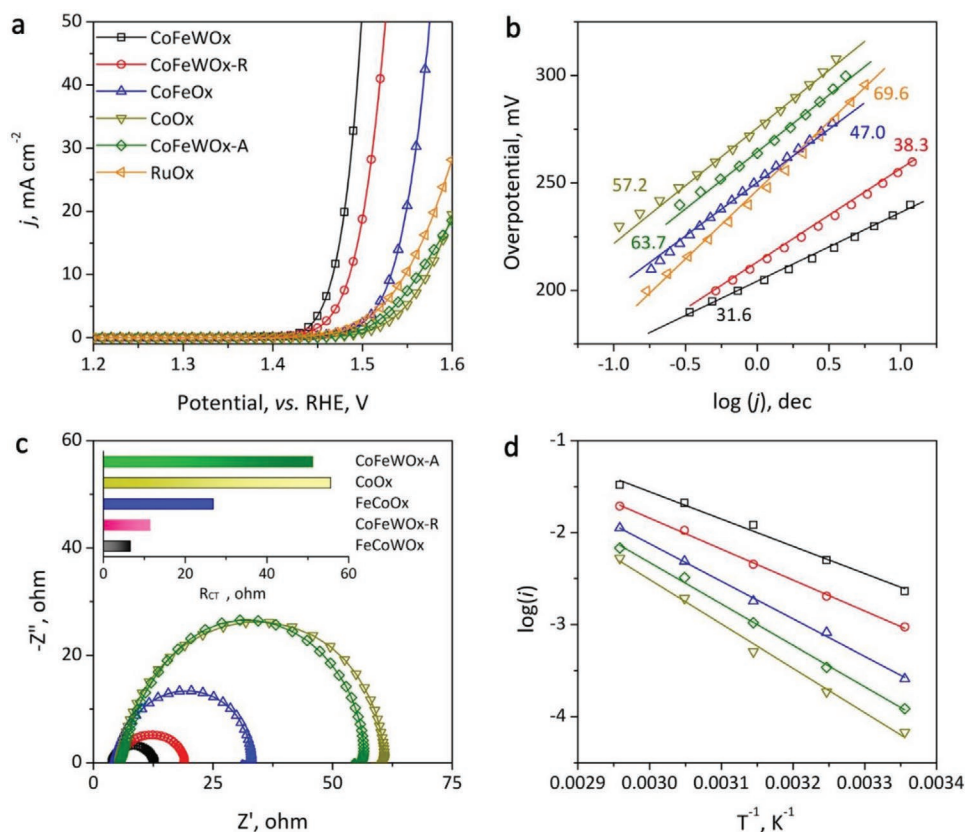


Figure 3. Catalytic performance of catalysts deposited on GCEs for OER in three-electrode configuration in 1 M KOH aqueous electrolyte. a) LSV curves, b) Tafel plots, c) EIS Nyquist plots ($\eta = 250 \text{ mV}$). d) Arrhenius plots of kinetic currents obtained at $\eta = 300 \text{ mV}$ on Au RDEs.

Table 1. OER catalytic performance parameters of FeCoWO_x and reference catalysts.

Catalysts	$\eta_{0}^{a)}$ [mV]	Tafel slope [mV dec ⁻¹]	Mass activity ^{b)} [A g ⁻¹]	TOF ^{c)} [s ⁻¹]	$R_{CT}^{d)}$ [Ω]	$E_a^{e)}$ [kJ mol ⁻¹]
CoFeWO _x	231	32	781.6	0.54	7.6	53
CoFeWO _x -R	249	38	391.5	0.28	11.4	58
CoFeO _x	303	47	45.5	0.014	26.8	74
CoO _x	342	57	13.4	0.0031	55.6	92
CoFeWO _x -A	332	64	20.7	0.012	51.2	86
RuO _x	324	70	31.6	0.011	–	–

^{a)}Obtained from LSV scans without *iR* correction; ^{b)}Obtained with 95% *iR* correction at $\eta = 300$ mV based on the total mass of catalysts; ^{c)}Obtained with 95% *iR* correction at $\eta = 300$ mV based on total 3d metals (Co/Fe) in catalysts; ^{d)}Determined at $\eta = 250$ mV; ^{e)}Obtained with 95% *iR* correction at $\eta = 250$ mV on Au RDEs.

Figure S15 (Supporting Information) shows that the trend observed for catalytic activity based on normalized current density is similar to what is displayed in Figure 3a. This confirms that the observed variance in the catalytic activity of the catalysts originates from their intrinsic catalytic activity rather than their different specific surface areas. In particular, CoFeWO_x and CoFeWO_x-R have similar morphology and elemental composition. The observed difference in their catalytic activity can be directly attributed to the higher abundance of Co_{Oh}³⁺ in CoFeWO_x, which serves as active catalytic sites for OER.^[8a,b]

The catalytic activity of the catalysts was further compared based upon their mass-based activities and turnover frequencies (TOFs). Details of these methods are described in the Experimental Section. The results are listed in Table 1 and Table S4 (Supporting Information). At η of 300 mV, CoFeWO_x delivers a mass-based activity of 781.6 A g⁻¹ (based on the total mass of the catalyst) and a TOF of 0.57 s⁻¹ (assuming all 3d metals are active), which is nearly two times higher than that of CoFeWO_x-R (391.5 A g⁻¹ and 0.29 s⁻¹). The TOF was also calculated based on the total moles of surface 3d metals, determined from cathodic peaks in cyclic voltammetry curves of catalysts at 1.3–1.4 V versus RHE (see Figure S16, Supporting Information). The TOF of CoFeWO_x is 1.96 s⁻¹, which is much higher than that of previously reported Co–Fe–W oxyhydroxides (1.5 s⁻¹).^[5c] In comparison, CoFeWO_x-R displays a TOF of 1.19 s⁻¹, which is similar to the previously reported value.

The kinetic performance of the catalysts was evaluated by their Tafel plots, as shown in Figure 3b.^[16] CoFeWO_x exhibits superior kinetic performance with the smallest Tafel slope of 32 mV dec⁻¹. CoFeWO_x-R has a similar kinetic performance with a slightly larger slope of 38 mV dec⁻¹. The Tafel slopes of the other reference and commercial RuO₂ catalysts are between 47 and 70 mV dec⁻¹, indicating that a chemical step (formation of an OOH* intermediate) after an electrochemical pre-equilibrium reaction is the OER rate-determining step (RDS).^[17] CoFeWO_x also displays the lowest charge transfer resistance (R_{CT}) and the highest near-surface carrier density as extracted from EIS measurements. Under an overpotential of 250 mV, the R_{CT} of CoFeWO_x at 6.6 Ω is smaller than that of CoFeWO_x-R at 11.4 Ω and CoFeWO_x-A at 51.2 Ω . From the Mott–Schottky plots (Figure S17, Supporting Information),^[18] the near-surface carrier density of CoFeWO_x (19.5×10^{19} cm⁻³) is 30% higher than that of CoFeWO_x-R (13.8×10^{19} cm⁻³). It is nearly four times greater than that of the crystalline phase segregated CoFeWO_x-A (5.1×10^{19} cm⁻³). The high surface carrier density can be attributed to their amorphous crystalline structure^[19] and

the abundant Co³⁺ in octahedral coordination.^[20] The higher carrier density is expected to facilitate fast electron transfer and improve OER performance. We also measured the apparent OER activation energy (E_a) of the catalysts (Figure S18, Supporting Information). Figure 3d shows that CoFeWO_x has the lowest E_a of 53 kJ mol⁻¹ (see Table 1), further confirming its superior OER activity.

To better understand the OER mechanisms on CoFeWO_x, we used in operando EIS and FTACV to investigate the role of Co_{Oh}³⁺ sites on the superior OER catalytic activity of CoFeWO_x in comparison with several other catalysts. The in operando Bode plots of the catalysts were collected under applied potentials from 1.03 to 1.68 V versus RHE as displayed in Figure S19 (Supporting Information) along with the corresponding Nyquist plots. Figure 4a displays 2D contour Bode plots of CoFeWO_x and reference catalysts. The peak loci of phase angles are marked by dashed arrows on the plots to distinguish OH⁻ adsorption sites and identify the OER active Co coordination geometries.^[15] The structure-defined spinel Co₃O₄ displays two distinctive loci between 0.1 and 10 Hz, and 30–5 $\times 10^3$ Hz, which can be assigned to Co_{Td} and Co_{Oh} sites, respectively.^[15] CoFeWO_x and CoO_x also have both Co_{Td} and Co_{Oh} loci, similar to those in Co₃O₄, which agree with the EXAFS results in Figure 1f, confirming the co-existence of Co_{Oh} and Co_{Td} in CoFeO_x and CoO_x.^[21] In contrast, CoFeWO_x exhibits a single-phase angle peak locus decaying at 20–5 $\times 10^3$ Hz, suggesting that OER is primarily initiated at Co_{Oh}. It should be noted that the locus of CoFeWO_x is similar to that of spinel ZnCo₂O₄, in which Co_{Oh} is the only active catalytic site (see Figure S20, Supporting Information).^[15,22] Further, CoFeWO_x-R has a similar single locus as that of CoFeWO_x.

The high-order harmonic components (≥ 4) in FTACV avoid the non-Faradaic process and signify currents related to electron transfer and catalytic reactions (Figure S21, Supporting Information).^[23] Thus, the 6th harmonic FTACV components of CoFeWO_x and reference catalysts at 10 Hz and 100 mV are compared in Figure 4b. Three distinctive sets of peaks can be assigned to different electron transfer steps along the OER pathway.^[17,22a,23b] Region I (1–1.2 V vs RHE) and II (1.2–1.5 V vs RHE) can be assigned to the redox of Co^{2+/3+} and the subsequent structure rearrangement toward the formation of Co^{3+/4+} active center, respectively.^[8b,17,24] The region beyond 1.5 V (region III) is associated with the fast water dissociation and O₂ production under a high overpotential.^[17,23b] CoFeWO_x has a very low Co^{2+/3+} redox current in the region I, which can be attributed to its high Co³⁺ abundance, where few Co²⁺ sites

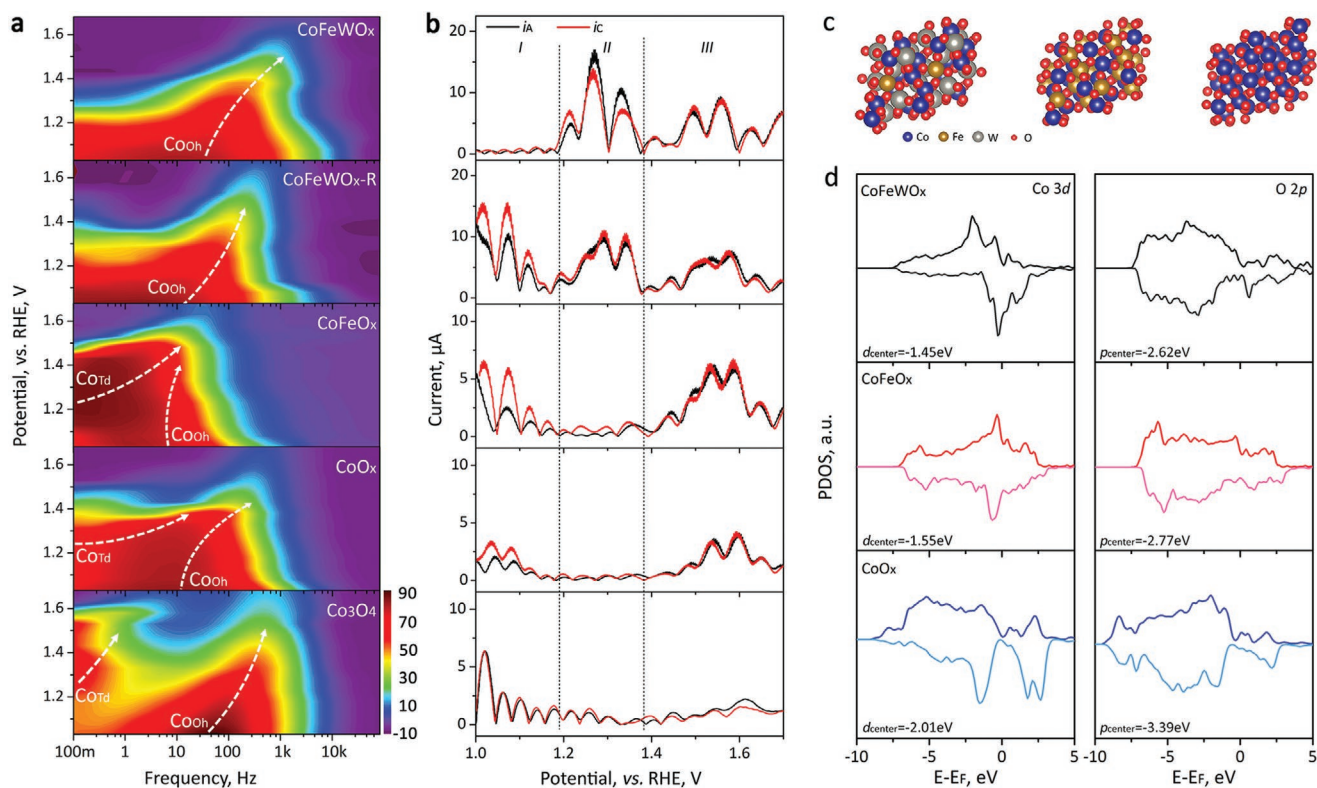


Figure 4. OER mechanistic studies by in operando EIS, FTACV and theoretical calculations. a) In operando 2D contour Bode plots and b) the 6th harmonic FTACV curves of catalysts. c) Illustrations of optimized DFT models (left: CoFeWO_x, middle: CoFeO_x, right: CoO_x) and d) the calculated Co3d and O2p PDOS.

are oxidized to Co³⁺. In contrast, other reference catalysts have higher Co^{2+/3+} redox currents in the region I, suggesting that Co²⁺ is oxidized to Co³⁺ as active catalytic sites for OER. Importantly, CoFeWO_x with abundant pre-generated Co³⁺ sites exhibits nearly two-times higher current ($\approx 17 \mu\text{A}$) in the region II than that of CoFeWO_x-R ($\approx 9 \mu\text{A}$). This observation is indicative of its faster structural transformation toward the Co^{3+/4+} active center, which is beneficial for the fast OER process. It should be noted that the redox of Fe^{3+/4+} ($\approx 1.9 \text{ V}$ vs Ag/AgCl) only overlaps with the rapid catalytic water oxidation in the region III.^[25] Additionally, the redox of W^{5+/6+} in WO₃ ($\approx 0.35 \text{ V}$ vs RHE) is also outside our tested potential window from 1.0 to 1.7 V versus RHE. Therefore, we can rule out any contribution from Fe and W to the measured currents in FTACV.^[26]

The intensity of measured currents in FTACV is correlated with the reaction rate on our catalysts. We further examined the kinetics of OER to determine the potential RDS.^[23b] CoFeWO_x has a relatively low current intensity in the region III, suggesting that the RDS of OER on CoFeWO_x is the formation of the O₂* intermediate, agreeing with its small Tafel slope of 32 mV dec⁻¹ (Table 1).^[16b,27] In comparison, CoFeO_x, CoO_x, and Co₃O₄ exhibit a much lower current in region II. This indicates that the formation of OOH* is the RDS,^[17,22a,28] agreeing with their higher Tafel slopes of 50–70 mV dec⁻¹.

DFT calculations were carried out to understand how electronic interactions among different metal elements in CoFeWO_x contribute to its excellent catalytic activity. Figure 4c

illustrates three models used for the calculations. The three oxide surfaces (CoFeWO_x, CoFeO_x, and CoO_x) were modeled as two-layer (221) slabs. The surface of the CoFeWO_x was modeled by replacing two W atoms with Fe on the surface of CoWO₄. Figure S22 (Supporting Information) displays the projected density of states (PDOS) of Co, Fe, W, and O in the three models. The Co3d electrons are the main contributor to the PDOS near the Fermi level, suggesting that Co would have higher activity in CoFeWO_x.^[29] Figure 4d compares the PDOS of Co3d and O2p electrons of the three models. The incorporation of Fe and W gradually tunes the electronic structures of Co and O. The *d*-band center of Co is shifted upward from -2.01 eV in the monometallic CoO_x model to -1.55 eV after doping Fe in the CoFeO_x model, which is further lifted to -1.45 eV in the CoFeWO_x model. This up-shift in the *d*-band center is expected to strengthen the adsorbate binding energies at Co sites, leading to more favorable OER thermodynamics.^[30] Therefore, the modulation of the *d*-band center of Co can optimize the interaction between Co and OER intermediates, resulting in improved catalytic activity for OER.^[31] Meanwhile, Figure 4d also shows that O *p*-electrons are lifted closer to their Fermi level, which is beneficial for improving the antibonding state and promoting catalytic activity for OER.^[8a,32] The calculated energy gaps between Co *d*-band and O *p*-band centers show a declining trend with 1.17 eV in CoFeWO_x, 1.22 eV in CoFeO_x, and 1.31 eV in CoO_x, indicating a lower electron transfer resistance in CoFeWO_x, which is also beneficial in promoting catalytic activity for OER.^[5b,33]

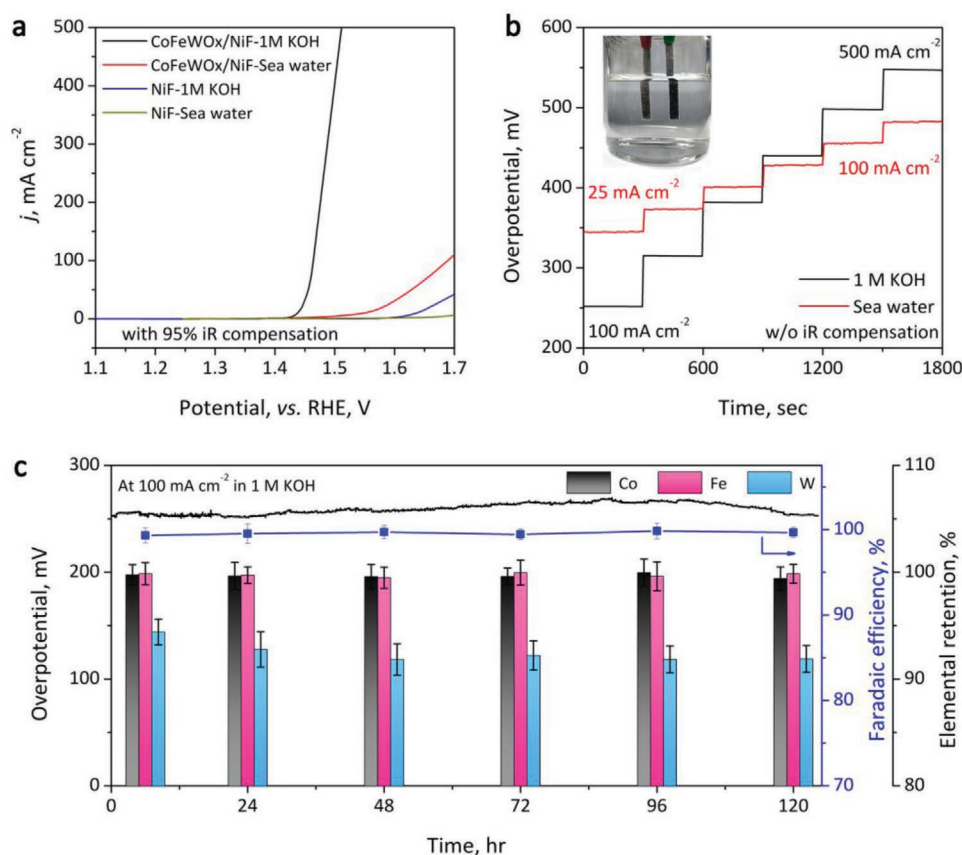


Figure 5. a) LSV polarization curves of $\text{FeCoWO}_x/\text{NiF}$ electrodes in three-electron configuration in 1 M KOH and seawater electrolyte. b) Multi-current responses of a two-electrode water electrolyzer using $\text{CoFeWO}_x/\text{NiF}$ and $\text{NiMoO}_4/\text{NiF}$ electrodes in 1 M KOH and seawater electrolyte. c) Stability test of the electrolyzer performed at 100 mA cm^{-2} in 1 M KOH electrolyte. The elemental retention of Co, Fe, and W in $\text{FeCoWO}_x/\text{NiF}$ during the electrolysis.

To demonstrate the practical application potential of FeCoWO_x , we tested the performance of CoFeWO_x directly electrodepositing on NiFs (denoted as $\text{CoFeWO}_x/\text{NiF}$). Figure 5a shows that the LSV curve of $\text{CoFeWO}_x/\text{NiF}$ measured in a three-electron configuration in 1 M KOH electrolyte has a rapid current increment. In contrast, the bare NiF displays negligible catalytic activity. $\text{CoFeWO}_x/\text{NiF}$ requires an overpotential of 211 mV to reach the current density of 10 mA cm^{-2} . It delivers 100 mA cm^{-2} at 234 mV and 500 mA cm^{-2} at 280 mV, outperforming most recently reported earth-abundant transition metal-based OER catalyst electrodes (see the detailed comparison in Table S5, Supporting Information). Furthermore, $\text{CoFeWO}_x/\text{NiF}$ can also work in near-neutral seawater electrolyte (pH = 8.4, conductivity = 32 mS cm^{-1}), requiring an overpotential of 422 mV to deliver the current density of 100 mA cm^{-2} .

A two-electrode water electrolyzer was assembled using $\text{CoFeWO}_x/\text{NiF}$ as the anode and a $\text{NiMoO}_4/\text{NiF}$ electrode (Figure S23, Supporting Information)^[34] as the cathode. As shown in Figure 5b, multi-step chronopotentiometric tests performed in both 1 M KOH and seawater electrolyte exhibit fast and steady responses, and generated gas bubbles can quickly dissipate from the electrode surfaces (see the inset image of Figure 5b). The stability of $\text{CoFeWO}_x/\text{NiF}$ was assessed by continuous discharge at 100 mA cm^{-2} for 120 h in 1 M KOH electrolyte. Figure 5c shows that the applied overpotential remains stable during the test, indicating excellent stability. The Faradaic

efficiency measured by quantifying O_2 produced using gas chromatography is close to 100% during the entire stability test. Periodic elemental analysis of the KOH electrolyte by ICP-AES confirms that there is minimum leaching of Co and Fe during the 120-h test. However, we found about 10 wt% of W was leached in the first 24 h of the electrolysis, and then the W content remained stable in the next 96 h. After the stability test, $\text{CoFeWO}_x/\text{NiF}$ shows minor morphological changes and remains amorphous without element/crystal phase segregations (see Figure S24, Supporting Information). XPS analysis of $\text{CoFeWO}_x/\text{NiF}$ after the stability test shows that the abundance of Co^{3+} increases from 72 to 85 at%. At the same time, the electronic structures of Fe and W are largely unchanged (Figure S25, Supporting Information). We further tested the stability of this $\text{CoFeWO}_x/\text{NiF}$ electrode in a 10 M KOH electrolyte at 80°C to simulate the working condition of practical alkaline water electrolyzers. The electrolyzer can work steadily during the 48-h test performed at 500 mA cm^{-2} , and the voltage has merely increased by $\approx 20 \text{ mV}$ (Figure S26, Supporting Information). Meanwhile, similar elemental retention performance can be observed.

3. Conclusion

In summary, we demonstrate an efficient synthetic method to electrodeposit trimetallic Co–Fe–W oxyhydroxides enriched

with Co^{3+} . The in situ oxidation by peroxide ligands released from $\text{WO}_4(\text{O}_2)^{4-}$ precursors play a crucial role in obtaining a high abundance of Co^{3+} . Spectroscopic characterization reveals that 72 at% of Co occupied the catalytic active octahedral coordinated $\text{Co}_{\text{Oh}}^{3+}$ site in CoFeWO_x . On a glassy carbon RDE, the high Co^{3+} abundance renders extraordinary OER performance with an ultralow overpotential of 231 mV at 10 mA cm^{-2} , a fast reaction kinetics with a low Tafel slope of 32 mV dec^{-1} , and a high TOF of 1.96 s^{-1} per surface 3d metal in 1 M KOH electrolyte, outperforming most of the recently reported earth-abundant transition metals based OER catalysts. The mechanistic investigation by in operando EIS and FTACV analysis indicates that abundant $\text{Co}_{\text{Oh}}^{3+}$ sites are highly active catalytic sites for OER. DFT calculation results show the optimization of Co electronic structures by Fe and W. Benefiting from the excellent intrinsic catalytic activity and hierarchical pore structures, $\text{CoFeWO}_x/\text{NiF}$ electrodes deliver a current density of 500 mA cm^{-2} at an overpotential of 280 mV in 1 M KOH and exhibit excellent durability under a large current density of 100 mA cm^{-2} over 120 h. This work demonstrates an easily scalable approach for fabricating high-performance OER electrodes for practical water electrolysis.

4. Experimental Section

Electrodeposition: Na_2WO_4 , $\text{Fe}(\text{NO}_3)_3$, and $\text{Co}(\text{NO}_3)_2$ (Sigma-Aldrich) was dissolved separately in deionized (DI) water as 0.2 M stock solutions to prepare the electrodeposition bath. First, H_2O_2 (30 w/w%) was added to the Na_2WO_4 stock solution under stirring with equal moles of H_2O_2 and Na_2WO_4 . The mixture was further stirred for 30 min before $\text{Fe}(\text{NO}_3)_3$ and $\text{Co}(\text{NO}_3)_2$ stock solutions were added. The final molar concentration of Co^{2+} , Fe^{3+} , and WO_4^{2-} in the electrodeposition bath was kept at 20, 5, and 20×10^{-3} M, respectively, and its pH was adjusted to 1.5 by adding 3 M HNO_3 . The NiFs were cleaned by bath sonication in acetone for 15 min and then rinsed with DI water. After drying, the NiFs were further bath sonicated in 0.1 M HCl for 15 min to remove surface oxide layers. The electrodeposition of CoFeWO_x on cleaned NiFs was carried out in the three-electrode configuration using a Pt mesh and an Ag/AgCl (saturated KCl) electrode as the counter and reference electrodes, respectively. The deposition was limited to a 2×2 cm^2 area, and the region adjacent to the electrodeposition area was sealed by a waterproof sealant, as illustrated in Figure 1b. The potential of -0.2 V versus Ag/AgCl was applied to NiFs for 10 min using an electrochemical workstation (CHI, 660E). After electrodeposition, NiFs were rinsed with DI water and dried in an oven overnight.

$\text{CoFeWO}_x\text{-R}$ was prepared by adding 20×10^{-3} M ascorbic acid to the electrodeposition bath (the concentration of ascorbic acid was optimized as described in the Supporting Information). Although $\text{WO}_4(\text{O}_2)^{4-}$ was stable in solutions containing a small amount of citric acid, O_2^{2-} would be competitively consumed by ascorbic acid and Co^{2+} , resulting in lower Co^{3+} concentration. Further, bimetallic CoFeO_x and monometallic CoO_x were also prepared under the same electrodeposition condition. However, the electrodeposition condition bath was changed to have 20×10^{-3} M Co^{2+} and 5×10^{-3} M Fe^{3+} or only 20×10^{-3} M Co^{2+} , respectively.

Materials Characterization: SEM imaging and EDX were performed on an SEM (Zeiss Ultra Plus). TEM images of samples deposited on Cu grids were taken on a TEM (FEI Themis Z). EELS spectra were collected on another TEM (Joel JEM-2100) at 200 kV. The surface area was measured by liquid N_2 physisorption on a surface analyzer (QuantaChrome, Autosorb-1). BET and BJH methods were used to calculate the specific surface area and pore size distribution, respectively. XRD patterns were recorded on an X-ray diffractometer (Shimadzu XRD-6000). XPS spectra were measured using an XPS spectrometer (Thermo Fisher, K-Alpha+) equipped with an Al-K α (1486.3 eV) radiation source. XAS spectra were

collected on the beamline BL-12B2 in the fluorescence mode at National Synchrotron Radiation Research Center (NSRRC, Taiwan). Data analysis and fitting were performed by the Demeter Software package using the FEFF 9.0 code.

Working Electrode Preparation: Catalyst ink at the concentration of 5 mg mL^{-1} was prepared by dispersing the catalyst (removed from NiFs) in a water/isopropanol ($v/v = 1/9$) solution containing 0.05 wt% Nafion 117. The ink was then dropped cast on GCEs (Pine instrument, 5 mm in diameter) with an areal mass loading of 0.2 mg cm^{-2} . The catalytic performance of catalysts was tested in the three-electrode configuration in O_2 saturated 1 M KOH electrolyte on an electrochemical workstation (CHI 760E), using a Pt mesh and a saturated Ag/AgCl electrode as counter and reference electrodes, respectively. A water circulator controlled the electrolyte temperature in a jacketed electrochemical cell. All measured potentials were corrected to the RHE by adding $E^0(\text{Ag}/\text{AgCl}) + 0.0591 \times \text{pH}$. The Ag/AgCl reference electrode was also calibrated in the three-electrode configuration using Pt foils (99.9%, Sigma-Aldrich) as working and counter electrodes in 0.5 M H_2SO_4 electrolyte saturated with 99.99% H_2 . CV scans were performed between -100 and $+100$ mV to catalyze HER and hydrogen oxidation reaction. The average zero current points were used to calibrate the Ag/AgCl reference electrode. It should be noted that the filling electrolyte in Ag/AgCl reference electrodes was replaced and performed calibration to minimize their drifting. The catalysts using a 1 M KOH Hg/HgO reference electrode were tested. The LSV curves obtained after averaging three-consecutive tests by using the two different types of reference electrodes overlapped. It was concluded that the results were not affected by the stability of Ag/AgCl reference electrodes, as reported in some other studies. The apparent activation energy was estimated from temperature-dependent catalytic activity, which used catalyst loaded Au rotary disk electrodes (Pine instrument, 5 mm in diameter). Catalysts deposited on NiFs (with a geometric surface area of ≈ 0.5 cm^2) were also directly used as working electrodes to measure their electrocatalytic performance. It should be noted that NiFs were fully covered by deposited materials. No bare NiFs were exposed to electrolytes after the electrodeposition. Thus, NiFs themselves unlikely directly catalyzed OER in the following OER performance tests using NiF electrodes.

Electrocatalytic Performance Test: Electrodes were first scanned for 10 cycles between $1\text{--}1.6$ V versus RHE at a scan rate of 100 mV s^{-1} to stabilize catalysts. Next, LSV and Tafel plots were collected under the scan rate of 2 mV s^{-1} with or without a 95%-iR correction. Nyquist plots were obtained under an overpotential of 250 mV. ECSA of catalysts loaded on GCEs was estimated by their CV scans in a non-Faradaic region in 1 M KOH electrolyte at scan rates from 2 to 50 mV s^{-1} . The cathodic and anodic currents at the mid-point were fitted linearly. The average absolute slopes were used as their double-layer capacitance (C_{dl}). A specific capacitance (C_s) of 0.04 mF cm^{-2} for metal oxides was used. ECSA was estimated by the ratio of C_{dl} to C_s . In operando Bode plots were collected at 1.03–1.68 V (vs RHE) with a step of 0.05 V at an amplitude of 5 mV from 10^5 to 0.1 Hz. FTACV was performed from -0.1 to 0.7 V versus Ag/AgCl electrode under a potential amplitude of 100 mV and an AC frequency of 10 Hz. The first to the 6th harmonic transformed $i\text{--}V$ curve was derived from 32 768 data points collected using the CHI software.

Carrier Density Calculation: The carrier density in Co catalysts and commercial Co_3O_4 crystalline nanoparticles were determined by EIS, which was performed at applied potentials from 0 to 0.4 V (vs Ag/AgCl). Capacitance was calculated at 0.1 Hz and plotted against the potential to develop the Mott–Schottky plot. The fitted slope of the linear part was used to calculate the carrier density by Equation (5):

$$\frac{1}{C_d} = \frac{2}{\epsilon \epsilon_0 N_A} \left(V - V_f - \frac{kT}{e} \right) \quad (5)$$

C_d was calculated by dividing C with measured ECSA, e is the charge of an electron (1.602×10^{-19} C), ϵ_0 is the free space permittivity (8.85×10^{-14} F cm^{-1}), and ϵ is the dielectric constant of metal oxides (an estimated value of 20 was used).

Turnover Frequency: TOF of catalysts was calculated by Equation (6):

$$\text{TOF} = \frac{i \times E_F}{4 \times F \times n} \quad (6)$$

where i (A) is the current obtained under the overpotential of 300 mV, E_F is the Faradaic efficiency, and F is Faraday constant ($96\,485\text{ C mol}^{-1}$). n is the molar number of Fe or Co catalytic active sites, which was estimated by two methods. The first method was based on the total mass loading of catalysts, which would provide underestimated TOF values by Equation (7):

$$n_{\text{CoFe}} = \frac{4 \times 10^{-5} \times (r_{\text{Co/Fe}} + 1)}{M_w} \quad (7)$$

where 4×10^{-5} (g) is the total mass of the catalyst; $r_{\text{Fe/Co}}$ is the molar ratio of Fe and Co in catalysts; and M_w is the molar mass of catalysts determined by EDX elemental analysis.

The second method was based on the assumption that all surface Co and Fe atoms are active sites. One-electron redox reactions for Co and Fe were assumed, the number of active 3d metal surface sites (n_{CoFe}) was calculated from redox features of $\text{Co}^{3+}/\text{Co}^{4+}$ in CV scans by Equation (8):

$$n_{\text{CoFe}} = \frac{Q_{\text{Co}^{3+}/\text{Co}^{4+}}}{F} \times (r_{\text{Co/Fe}} + 1) \quad (8)$$

where Q is the amount of charge from the $\text{Co}^{3+}/\text{Co}^{4+}$ redox peak, F is Faraday constant.

Apparent Activation Energy: The apparent enthalpy of activation (ΔH^* , can be simply treated as the activation energy, E_a) of catalysts was determined by temperature-dependent measurements. The experiments were carried out in the water-jacketed electrochemical cell, and its temperature was controlled by a water circulator. A thermal meter was submerged in electrolytes to measure their temperature. The cell was sealed to minimize evaporation. LSV curves were recorded at 2 mV s^{-1} and corrected with 95% of internal resistances as determined from EIS measurement at 0 V. The current obtained at $\eta = 300\text{ mV}$ was used to calculate ΔH^* of various electrocatalysts using the Arrhenius equation:

$$k = A e^{-E_a/RT} \quad (9)$$

where k is the reaction rate, as represented by the current (i_k) obtained from the electrochemical test. A is a pre-factor for a given chemical reaction. R is the gas constant ($8.314\text{ J mol}^{-1}\text{ K}^{-1}$), and T is the temperature. The equation can be reorganized as:

$$\frac{\partial(\log(i_k))}{\partial\left(\frac{1}{T}\right)} \Big|_{\eta} = -\frac{\Delta H}{2.3R} \quad (10)$$

The slope obtained by the linear fitting of $\log(i_k)$ against $1/T$ can be used to calculate ΔH .

Computational Method: All DFT calculations were performed using the VASP code including spin-polarization. DFT+U was used to describe the on-site Coulomb interaction of localized electrons, with U_{eff} values of 3.32, 5.30, and 6.20 eV for Co, Fe, and W, respectively. Core electrons were described by the projector augmented wave method.^[35] Electronic exchange and correlation were described by the generalized gradient approximation method with the functional developed by Perdew, Burke, and Ernzerhof.^[36] Valence electrons were described by the Kohn–Sham wave functions expanded in a plane wave basis^[37] with an energy cutoff set to 400 eV. Structures were considered relaxed when all the force on each atom was lower than 0.05 eV \AA^{-1} . The Brillouin zone was sampled by a $(3 \times 3 \times 1)$ k -point mesh via the Monkhorst–Pack method.^[38] Each calculated d - or p -band center value was the average of d -/ p -band centers of spin-up and spin-down

electrons. The band centers of the Co and O atoms in different models were calculated by:

$$\text{Band center} = \frac{\int_{-\infty}^{+\infty} (\varepsilon - E_F) n(\varepsilon) d\varepsilon}{\int_{-\infty}^{+\infty} n(\varepsilon) d\varepsilon} \quad (11)$$

where ε is the energy of state, E_F is the Fermi level, and n is the number of states.

Supporting Information

Supporting Information is available from the Wiley Online Library or from the author.

Acknowledgements

J.C. and H.L. contributed equally to this work. This work was supported by the Australian Research Council under the Future Fellowships scheme (FT160100107). The calculations were supported by the Welch Foundation (F-1841) and the Texas Advanced Computing Center.

Conflict of Interest

The authors declare no conflict of interest.

Keywords

cobalt oxyhydroxide, electrodeposition, oxygen evolution reaction, tungstate, water splitting

Received: August 11, 2020
Revised: September 22, 2020
Published online:

- [1] a) M. G. Walter, E. L. Warren, J. R. McKone, S. W. Boettcher, Q. Mi, E. A. Santori, N. S. Lewis, *Chem. Rev.* **2010**, *110*, 6446; b) M. Wang, Z. Wang, X. Gong, Z. Guo, *Renewable Sustainable Energy Rev.* **2014**, *29*, 573.
- [2] a) M. Carmo, D. L. Fritz, J. Mergel, D. Stolten, *Int. J. Hydrogen Energy* **2013**, *38*, 4901; b) K. Zeng, D. Zhang, *Prog. Energy Combust. Sci.* **2010**, *36*, 307.
- [3] T. R. Cook, D. K. Dogutan, S. Y. Reece, Y. Surendranath, T. S. Teets, D. G. Nocera, *Chem. Rev.* **2010**, *110*, 6474.
- [4] a) C. C. L. McCrory, S. Jung, J. C. Peters, T. F. Jaramillo, *J. Am. Chem. Soc.* **2013**, *135*, 16977; b) D. Chen, C. Chen, Z. M. Baiyee, Z. Shao, F. Ciucci, *Chem. Rev.* **2015**, *115*, 9869; c) L. Trotochaud, J. K. Ranney, K. N. Williams, S. W. Boettcher, *J. Am. Chem. Soc.* **2012**, *134*, 17253; d) R. D. L. Smith, M. S. Prévot, R. D. Fagan, S. Trudel, C. P. Berlinguette, *J. Am. Chem. Soc.* **2013**, *135*, 11580.
- [5] a) Z. W. Seh, J. Kibsgaard, C. F. Dickens, I. Chorkendorff, J. K. Nørskov, T. F. Jaramillo, *Science* **2017**, *355*, 4998; b) J. Suntivich, K. J. May, H. A. Gasteiger, J. B. Goodenough, Y. Shao-Horn, *Science* **2011**, *334*, 1383; c) B. Zhang, X. Zheng, O. Voznyy, R. Comin, M. Bajdich, M. García-Melchor, L. Han, J. Xu, M. Liu, L. Zheng, F. P. García de Arquer, C. T. Dinh, F. Fan, M. Yuan, E. Yassitepe, N. Chen, T. Regier, P. Liu, Y. Li, P. De Luna, A. Janmohamed, H. L. Xin, H. Yang, A. Vojvodic, E. H. Sargent, *Science* **2016**, *352*, 333.

- [6] a) A. S. Batchellor, S. W. Boettcher, *ACS Catal.* **2015**, *5*, 6680; b) M. S. Burke, M. G. Kast, L. Trotochaud, A. M. Smith, S. W. Boettcher, *J. Am. Chem. Soc.* **2015**, *137*, 3638; c) L. Wei, H. E. Karahan, S. Zhai, H. Liu, X. Chen, Z. Zhou, Y. Lei, Z. Liu, Y. Chen, *Adv. Mater.* **2017**, *29*, 1701410; d) J. Liu, Y. Ji, J. Nai, X. Niu, Y. Luo, L. Guo, S. Yang, *Energy Environ. Sci.* **2018**, *11*, 1736; e) M. B. Stevens, L. J. Enman, E. H. Korkus, J. Zaffran, C. D. M. Trang, J. Asbury, M. G. Kast, M. C. Toroker, S. W. Boettcher, *Nano Res.* **2019**, *12*, 2288.
- [7] a) P. M. S. Monk, S. L. Chester, *Electrochim. Acta* **1993**, *38*, 1521; b) Y. Pi, Q. Shao, P. Wang, F. Lv, S. Guo, J. Guo, X. Huang, *Angew. Chem., Int. Ed.* **2017**, *56*, 4502; c) P. F. Liu, S. Yang, L. R. Zheng, B. Zhang, H. G. Yang, *Chem. Sci.* **2017**, *8*, 3484.
- [8] a) T. Wu, S. Sun, J. Song, S. Xi, Y. Du, B. Chen, W. A. Sasangka, H. Liao, C. L. Gan, G. G. Scherer, L. Zeng, H. Wang, H. Li, A. Grimaud, Z. J. Xu, *Nat. Catal.* **2019**, *2*, 763; b) A. Bergmann, T. E. Jones, E. Martinez Moreno, D. Teschner, P. Chernev, M. Gliech, T. Reier, H. Dau, P. Strasser, *Nat. Catal.* **2018**, *1*, 711; c) Z. J. Xu, *Sci. China Mater.* **2020**, *63*, 3.
- [9] Y. Jiao, Y. Zheng, M. Jaroniec, S. Z. Qiao, *Chem. Soc. Rev.* **2015**, *44*, 2060.
- [10] X. Lu, C. Zhao, *Nat. Commun.* **2015**, *6*, 6616.
- [11] B. Q. Li, C. Tang, H. F. Wang, X. L. Zhu, Q. Zhang, *Sci. Adv.* **2016**, *2*, 1600495.
- [12] T. Pauporté, Y. Soldo-Olivier, R. Faure, *J. Phys. Chem. B* **2003**, *107*, 8861.
- [13] S. H. Ahn, I. Choi, H.-Y. Park, S. J. Hwang, S. J. Yoo, E. Cho, H.-J. Kim, D. Henkensmeier, S. W. Nam, S.-K. Kim, J. H. Jang, *Chem. Commun.* **2013**, *49*, 9323.
- [14] Z. L. Wang, J. S. Yin, Y. D. Jiang, *Micron* **2000**, *31*, 571.
- [15] H.-Y. Wang, S.-F. Hung, H.-Y. Chen, T.-S. Chan, H. M. Chen, B. Liu, *J. Am. Chem. Soc.* **2016**, *138*, 36.
- [16] a) J. O. M. Bockris, *J. Chem. Phys.* **1956**, *24*, 817; b) J. O. Bockris, T. Otagawa, *J. Phys. Chem.* **1983**, *87*, 2960.
- [17] J. B. Gerken, J. G. McAlpin, J. Y. C. Chen, M. L. Rigsby, W. H. Casey, R. D. Britt, S. S. Stahl, *J. Am. Chem. Soc.* **2011**, *133*, 14431.
- [18] M. Gleria, R. Memming, *J. Electroanal. Chem. Interfacial Electrochem.* **1975**, *65*, 163.
- [19] G. Cheng, T. Kou, J. Zhang, C. Si, H. Gao, Z. Zhang, *Nano Energy* **2017**, *38*, 155.
- [20] C. F. Windisch, K. F. Ferris, G. J. Exarhos, S. K. Sharma, *Thin Solid Films* **2002**, *420–421*, 89.
- [21] S. F. Hung, Y. Y. Hsu, C. J. Chang, C. S. Hsu, N. T. Suen, T. S. Chan, H. M. Chen, *Adv. Energy Mater.* **2018**, *8*, 1701686.
- [22] a) M. E. Lyons, M. P. Brandon, *Int. J. Electrochem. Sci.* **2008**, *3*, 1425; b) P. W. Menezes, A. Indra, A. Bergmann, P. Chernev, C. Walter, H. Dau, P. Strasser, M. Driess, *J. Mater. Chem. A* **2016**, *4*, 10014.
- [23] a) H. Adamson, A. M. Bond, A. Parkin, *Chem. Commun.* **2017**, *53*, 9519; b) Y. Liu, S.-X. Guo, L. Ding, C. A. Ohlin, A. M. Bond, J. Zhang, *ACS Appl. Mater. Interfaces* **2015**, *7*, 16632.
- [24] A. Bergmann, E. Martinez-Moreno, D. Teschner, P. Chernev, M. Gliech, J. F. de Araújo, T. Reier, H. Dau, P. Strasser, *Nat. Commun.* **2015**, *6*, 8625.
- [25] a) L. Fan, B. Zhang, B. J. J. Timmer, N. V. R. A. Dharanipragada, X. Sheng, C.-W. Tai, F. Zhang, T. Liu, Q. Meng, A. K. Inge, L. Sun, *Nano Energy* **2020**, *72*, 104656; b) J. Y. C. Chen, L. Dang, H. Liang, W. Bi, J. B. Gerken, S. Jin, E. E. Alp, S. S. Stahl, *J. Am. Chem. Soc.* **2015**, *137*, 15090.
- [26] a) S. Darmawi, S. Burkhardt, T. Leichtweiss, D. A. Weber, S. Wenzel, J. Janek, M. T. Elm, P. J. Klar, *Phys. Chem. Chem. Phys.* **2015**, *17*, 15903; b) G. Wünsch, *Talanta* **1980**, *27*, 649.
- [27] N. T. Suen, S. F. Hung, Q. Quan, N. Zhang, Y. J. Xu, H. M. Chen, *Chem. Soc. Rev.* **2017**, *46*, 337.
- [28] M. Bajdich, M. García-Mota, A. Vojvodic, J. K. Nørskov, A. T. Bell, *J. Am. Chem. Soc.* **2013**, *135*, 13521.
- [29] X. Zhang, B. Zhang, P. De Luna, Y. Liang, R. Comin, O. Voznyy, L. Han, F. P. García de Arquer, M. Liu, C. T. Dinh, T. Regier, J. J. Dynes, S. He, H. L. Xin, H. Peng, D. Prendergast, X. Du, E. H. Sargent, *Nat. Chem.* **2018**, *10*, 149.
- [30] J. Chen, H. Li, Z. Pei, Q. Huang, Z. Yuan, C. Wang, X. Liao, G. Henkelman, Y. Chen, L. Wei, *J. Mater. Chem. A* **2020**, *8*, 15951.
- [31] a) W. T. Hong, K. A. Stoerzinger, Y.-L. Lee, L. Giordano, A. Grimaud, A. M. Johnson, J. Hwang, E. J. Crumlin, W. Yang, Y. Shao-Horn, *Energy Environ. Sci.* **2017**, *10*, 2190; b) S. Bhattacharjee, U. V. Waghmare, S.-C. Lee, *Sci. Rep.* **2016**, *6*, 35916.
- [32] a) A. Grimaud, O. Diaz-Morales, B. Han, W. T. Hong, Y.-L. Lee, L. Giordano, K. A. Stoerzinger, M. T. M. Koper, Y. Shao-Horn, *Nat. Chem.* **2017**, *9*, 457; b) A. Grimaud, K. J. May, C. E. Carlton, Y.-L. Lee, M. Risch, W. T. Hong, J. Zhou, Y. Shao-Horn, *Nat. Commun.* **2013**, *4*, 2439.
- [33] Y. Zhou, S. Sun, J. Song, S. Xi, B. Chen, Y. Du, A. C. Fisher, F. Cheng, X. Wang, H. Zhang, Z. J. Xu, *Adv. Mater.* **2018**, *30*, 1802912.
- [34] J. Zhang, T. Wang, P. Liu, Z. Liao, S. Liu, X. Zhuang, M. Chen, E. Zschech, X. Feng, *Nat. Commun.* **2017**, *8*, 15437.
- [35] P. E. Blöchl, *Phys. Rev. B* **1994**, *50*, 17953.
- [36] J. P. Perdew, K. Burke, M. Ernzerhof, *Phys. Rev. Lett.* **1996**, *77*, 3865.
- [37] W. Kohn, L. J. Sham, *Phys. Rev.* **1965**, *140*, A1133.
- [38] H. J. Monkhorst, J. D. Pack, *Phys. Rev. B* **1976**, *13*, 5188.